J4.7 SYNTHETIC APERTURE RADAR OBSERVATIONS OF MESOSCALE ATMOSPHERIC PHENOMENA

George S. Young *
The Pennsylvania State University, University Park, Pennsylvania

Nathaniel S. Winstead, Frank M. Monaldo, Donald R. Thompson
The Johns Hopkins University Applied Physics Laboratory, Laurel, Maryland

Todd D. Sikora
Millersville University, Millersville, Pennsylvania

1. INTRODUCTION

Satellite-borne synthetic aperture radar (SAR) provides the capability of mapping over-water surface wind speed fields at resolutions of a kilometer or better (Monaldo et al. 2001, 2004). Thus, SAR provides an exceptionally high resolution tool for examining the mesoscale phenomena of the marine atmospheric boundary layer (Sikora et al. 2005; Young et al. 2005; Winstead et al. 2002). The signatures of mesoscale atmospheric phenomena commonly seen in SAR images include fronts, convection, gravity waves, and barrier effects. SAR observations allow one to identify these phenomena in otherwise data-sparse maritime regions and to study both their kinematic structure and their relationship to synoptic and topographic forcing features. This paper reviews a number of recent SAR observations from RADARSAT-1 (Pichel and Clemente-Colon 2001) as a means of illustrating the potential of this observational resource.

2. SYNTHETIC APERTURE RADAR

Synthetic aperture radar measures the surface wind speed in much the same way scatterometers do, by measuring the radar signal reflected by small waves on the ocean surface (Stoffelen and Anderson 1993, 1997). These waves grow in amplitude as the wind speed increases, thus increasing the radar back-scatter created through a Bragg-like resonance. Most SARs employ wavelengths on the order of 10^{-1} m, so the resonant waves are short enough to respond quickly to changes in the surface wind speed. This responsiveness, coupled with the high spatial resolution of most satellite-borne SARs allows these systems to image surface wind structures at very high resolution (order of magnitude 10 to 100 m).

The diagnosis of surface wind speed from normalized radar cross section is commonly undertaken using the semi-empirical scatterometer algorithms based on CMOD4 (e.g., Freilich and Dunbar 1993; Stoffelen and Anderson 1993) and CMOD5 (Hersbach 2003) algorithms. These algorithms, originally developed for vertically polarized satellite-borne scatterometers, must be modified somewhat for use with horizontally polarized SARs (Thompson and Beal 2000; Thompson et al. 2001). While the results compare well with in situ observations in most cases (e.g., Horstmann et al. 2003; Monaldo et al. 2001, 2004), significant errors can result from ocean currents, surfactant slicks, (Johannessen 1999) and non-neutral static stability in the atmospheric surface layer (Foster et al. 2004).

Moreover, the relationship between backscatter and wind speed depends upon the radar look direction relative to the wave crests. Thus, a SAR looking into the wind "sees" a much rougher sea than one looking across the wind. Assuming one of these situations when the other in fact is the case can result in a factor-of-2 error in the SAR-derived wind speed (Loescher et al. 2005; Sikora et al. 2006). Thus, a source of wind direction information is required before one can derive surface wind speed images from backscatter data. Satellite-born scatterometers such as the instrument aboard the QuikSCAT satellite (Weissman et al. 2002) neatly solve this problem by using multiple look directions, allowing one to simultaneously diagnose both the wind direction and speed. SAR sacrifices this capability however, as a result of the very antenna configuration that allows it to achieve much higher spatial resolution than that achieved by conventional scatterometers (Monaldo et al. 2004).

SAR users have turned to a variety of wind data sources to solve this problem. One can deduce the wind direction from the backscatter field itself by observing streaks and island wind shadows (e.g. Gerling 1986, Wackermann et al. 1996, Fetterer et al. 1998, Horstmann et al. 2000), one can utilize the courser-resolution wind directions available from nearly coincident scatterometer observations, or one can use numerical model analyses to provide the wind directions (Monaldo et al. 2001). The latter procedure offers the operational advantages of global coverage and objectivity, so it is employed in preparing the wind speed images discussed below. The model used for this study was NOGAPS (Monaldo et al. 2001) although others have proved equally appropriate.

3. MESOSCALE PHENOMENA

While SAR has proven capable of observing many oceanographic and meteorological phenomena we will

* *Corresponding author address:* George S. Young, Dept. of Meteorology, 503 Walker Building, University Park PA, 16802; e-mail: young@meteo.psu.edu

focus here on three broad classes which account for much of the mesoscale wind variability of interest to marine forecasters and their user communities. Fronts with their sharp wind shifts show prominently on SAR images, as do their mesoscale substructures. Likewise downdraft outflows from both shallow dry and deep moist convection are readily apparent in SAR imagery. Barrier effects, the third class of SAR-observed mesoscale phenomena to be discussed herein, are perhaps the most diverse. This class includes the broad range of phenomena that result from terrain blocking of stably stratified flow.

3.1 *Fronts*

Features observed on SAR images include the lobe and cleft instability of gravity currents, shear-driven vortices with scale depending largely on frontal type, and shear-driven gravity waves on the frontal inversion with orientation depending largely on frontal type (Young et al. 2005). Observation of these features can thus provide information on frontal type and behavior that would not otherwise be available in data-sparse marine regions. Frontal positions can also be determined much more precisely than is possible using courser-resolution scatterometer data.

Figure 1 shows the SAR image of a portion of a cold front. The front is progressing northeastward across the image, and is distorted at the surface by the series of bulges (lobes) and kinks (clefts) typical of the lobe and cleft instability common to gravity currents (Lee and Wilhelmson 1997). SAR imagery thus provides the opportunity to study this phenomenon for large segments of fronts, a proposition that would be much more challenging with surface-based or airborne Doppler weather radars.

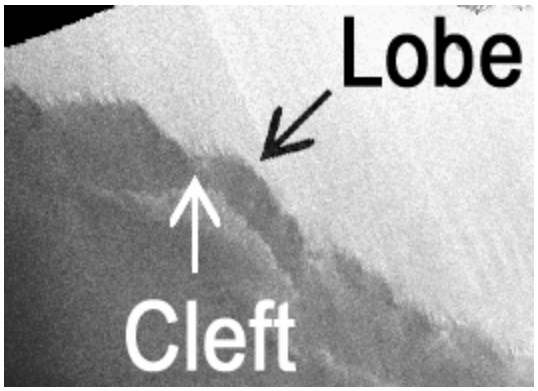

Figure 1. Portion of a RADARSAT-1 synthetic aperture radar image of an intense cold front moving northeastward near the Aleutian Islands, 5:06 UTC on February 08, 2001. Image is located near 58 N, 172 W. This sub-image shows detail of the lobe and cleft structure. (Provided courtesy of JHUAPL, © Canadian Space Agency)

Figure 2 shows a SAR image of another cold front, this one with a series of meso-γ-scale vortices spaced along the frontal discontinuity. The front is progressing southeastward and cyclonic shear across the front is self organizing via vortex wrap-up (Lee and Wilhelmson 1997; Parsons and Hobbs 1983). SAR provides a useful complement to the existing aircraft observations of this phenomena as it yields more detail of the frontal behavior in the vortex wrap-up regions. Shear-driven vortices are often seen on warm and occluded fronts as well, although typically of larger scale and with less tendency to wrap up. Because the observed shear magnitude is similar for the various types of fronts, it is conjectured that these differences in vortex behavior is a result in the difference in frontal slope between cold fronts (nearly vertical in the first kilometer or so) and warm and occluded fronts (gently sloping even near the surface).

The narrow bright line along the front in Figure 2 is probably a result of enhanced backscatter from the wave breaking events associated with a sudden shift in wind direction. Similarly, the enhanced brightness on the west side of each vortex probably reflects a change in wind direction rather than wind speed. This image thus provides a good example of both the potential for SAR wind-speed imagery and challenges posed by the complex interplay of air-sea interaction with radar backscatter physics.

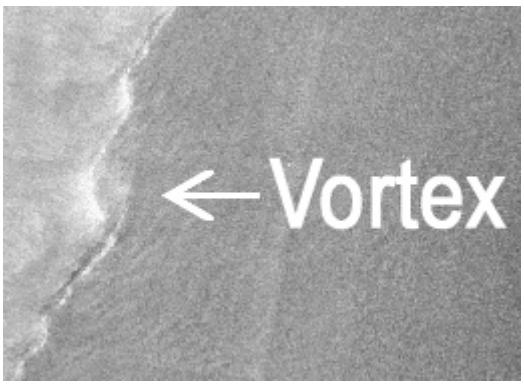

Figure 2. RADARSAT-1 synthetic aperture radar image of an southeastward moving cold front in the Gulf of Alaska, 15:45 UTZ on December 20, 2001. Image is located near 47 N, 143 W. This sub-image shows detail of the vortex structure. (Provided courtesy of JHUAPL, © Canadian Space Agency)

Figure 3 shows a portion of a warm front moving to the northeast. The shear between the fast, front-parallel winds ahead of the front (i.e. cold conveyor belt) and the southwesterly winds behind the front yields gravity waves on the frontal inversion when the warm air rides up over the cold. The waves align roughly perpendicular to the front, because they are shear-perpendicular and thus perpendicular to the thermal wind. The waves can be seen on the SAR imagery because they modulate the surface wind speed in those regions where the frontal zone is close enough to the sea surface (e.g., Vachon et al. 1995; Winstead et al. 2002). Thus, while the gravity waves may exist throughout a sheared frontal zone, they can be seen on the SAR image only within a few tens of kilometers of

the front's intersection with the sea surface. Similar waves are also common on occluded fronts. There appear to be less common on cold fronts and aligned more nearly parallel to the front, as ageostrophic flow creates much of the shear in cold frontal zones.

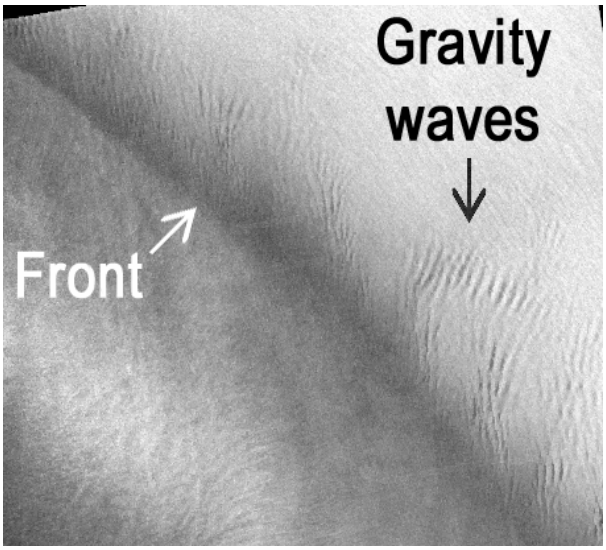

Figure 3. RADARSAT-1 synthetic aperture radar image of an occluded front with gravity waves in the Gulf of Alaska, 3:00 UTC on December 16, 2000. Image is located at 52 N, 139 W. (Provided courtesy of JHUAPL, © Canadian Space Agency)

3.2 *Convection*

Convection, both boundary layer and deep, causes downdrafts and surface outflows, which are readily apparent in SAR imagery and indicate the boundary layer stability even when the lower atmosphere if hidden by upper-level clouds (Sikora et al. 1995; Babin et al. 2003). Moreover, SAR images can be used to measure the size, shape, orientation, and gust intensity of the surface outflows from deep precipitating convection, again irrespective of the overlying cloud.

Figure 4 shows a SAR image of the surface outflow patterns associated with deep convection. The large horizontal scale of the outflows (tens of kilometers) confirms the diagnosis, while the orientation of the bright / dark (i.e. fast / slow) patterns indicates which way the gusts are moving. As with the vortices discussed above, however, these divergent patterns alter the wind direction thus further modifying the SAR-diagnosed wind speed pattern.

Figure 5 shows a SAR image of the surface wind speed pattern (gustiness) caused by a field of shallow, non-precipitating convection. The cells are much smaller and more densely packed than in the case of deep, precipitating convection (e.g. Figure 4). This difference is typical and serves as a good distinguishing feature.

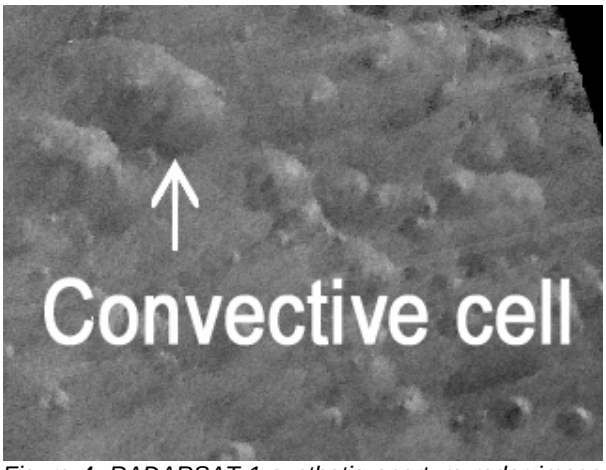

Figure 4. RADARSAT-1 synthetic aperture radar image of the surface outflows from precipitating convection in the Gulf of Alaska, 3:20 UTC on January 12, 2003. Image is located near 53 N, 144 W. (Provided courtesy of JHUAPL, © Canadian Space Agency)

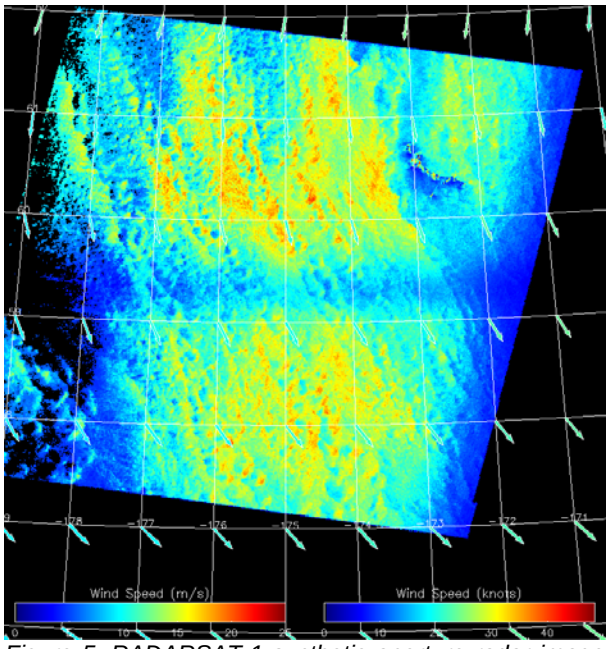

Figure 5. RADARSAT-1 synthetic aperture radar image of the surface wind speed pattern caused by a field of shallow non-precipitating convection in the Bering Sea, 4:41 UTC on December 22, 1999. Image is located near 55 N, 166 W. (Provided courtesy of JHUAPL)

3.3 *Barrier Effects*

Mesoscale barrier effects in both the boundary layer and free troposphere strongly affect the surface wind speed field (Winstead et al. 2002; Loescher et al. 2005), so SAR images contain the signatures of mountain lee waves, island wakes, gap flow, and barrier jets. Because these phenomena often coexist offshore of mountainous coasts, SAR images can be used to study their interaction. An example of this type of interaction is the modulation of island wakes and gap

flow by mountain waves in the Kennedy Entrance region of the Alaskan coast.

Figure 6 shows a SAR image of gravity waves in the lee of a quasi-linear mountain crest. As with the shear-driven discussed above, the waves ride a layer of increased static stability aloft but impose a noticeable modulation on the surface wind field. The high-resolution wind imagery provided by SAR satellites allows this mesoscale wind variation to be quantified, yielding information that could potentially be used to infer wave intensity and thus the degree of aviation hazard they pose.

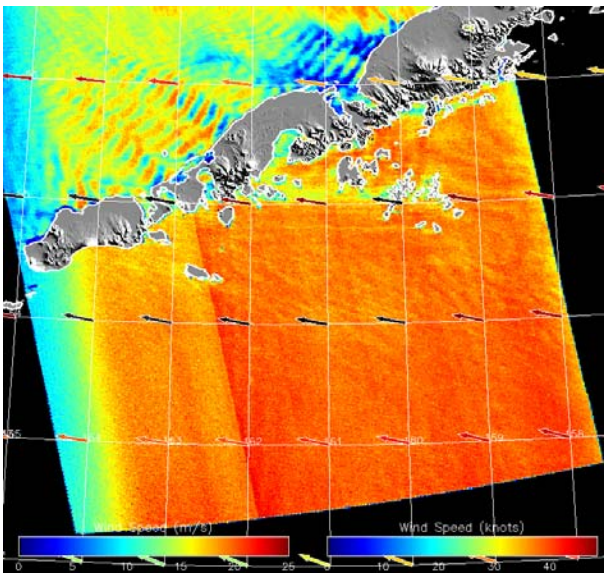

Figure 6. RADARSAT-1 synthetic aperture radar image of the surface wind speed pattern caused by a field of orographically generated gravity waves over the Bering sea, 4:28 UTC on February 23, 2001. Image is located near 57 N, 163 W. (Provided courtesy of JHUAPL)

Figure 7 shows a SAR image of gravity waves generated by an isolated peak. They form a chevron pattern of enhanced and suppressed surface wind speed with the point of the V directed upwind. Interference patters between the waves from nearby peaks are frequently observed, a phenomenon that increases the challenge of forecasting maximum wind speed in lee of mountainous coasts.

Figure 8 shows a SAR wind speed image (Monaldo et al. 2004) containing both horizontally propagating orographic gravity waves and low-speed island wakes, the latter resulting from wave breaking and enhanced orographic drag (Schär and Smith 1993). The two phenomena represent different Froude number regimes and thus must be originating from different orographic features. In this case the horizontally propagating mountain waves are being generated by flow over the coastal mountains of the Alaskan mainland while the low-speed wakes are being generated by low-altitude wave breaking over the Barren islands.

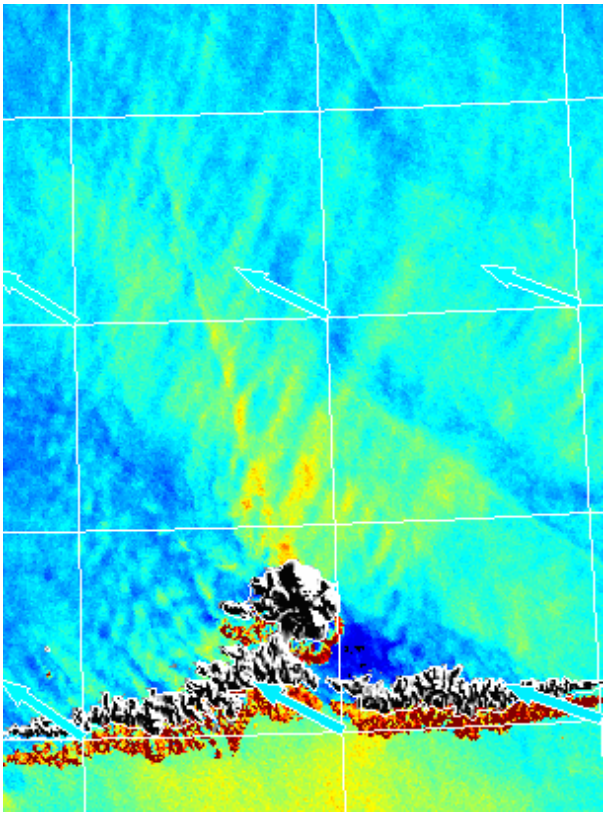

Figure 7. RADARSAT-1 synthetic aperture radar image of the surface wind speed pattern caused by a field of orographically generated gravity waves over the Bering Sea, down wind of an isolated volcanic peak, 5:34 UTC on Marsh 20, 2005. Image is located near 53 N, 174 W. (Provided courtesy of JHUAPL)

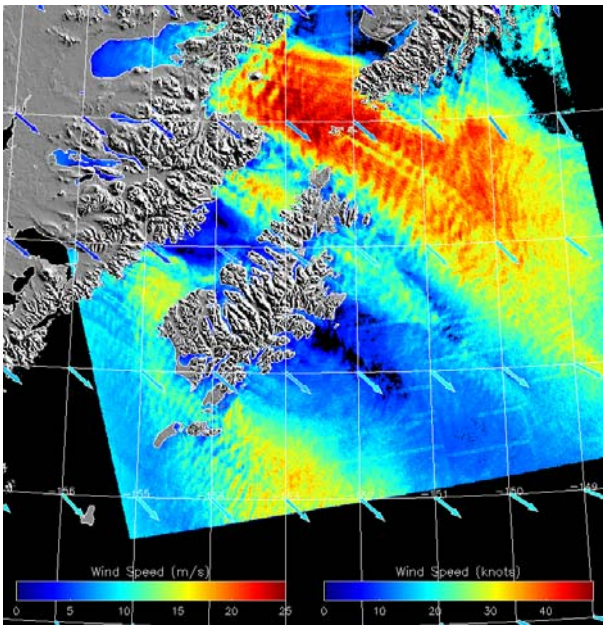

Figure 8. RADARSAT-1 synthetic aperture radar-derived wind speed image showing the pattern caused by a field of orographically generated gravity waves over

the Gulf of Alaska, 3:48 UTC on September 30, 2000 Image is located near 59 N, 152 W. (Provided courtesy of JHUAPL)

4. CONCLUSIONS

Synthetic aperture radar aboard polar orbiting satellites offers a unique imaging capability for surface wind speed over the sea. The combination of high spatial resolution and all-weather capability allow SAR to observe numerous meso-γ and meso-β-scale phenomena that are below the resolution of conventional scatterometers. The existence and structure of these small-scale phenomena tell the analyst much about the larger scale atmospheric structure that could not be deduced directly from coarser-resolution remote sensors. While visible satellite imagery offers resolution comparable to SAR, it does not provide an all-weather capability for viewing surface weather phenomena as mid and upper-level clouds can obscure the view. Moreover, SAR imagery can document wind patterns such as dry convection that have no associated cloud patterns.

SAR image analysis also poses a number of challenges. The current polar orbiting satellites provide only occasional coverage, making the tool more useful for mesoscale research than operational forecasting. Moreover the complexity of the relation between wind-driven sea state and radar backscatter makes interpretation of SAR images difficult in the presence of highly variable wind directions. This difficulty is probably no greater, however, than that associated with the interpretation of infrared water vapor imagery, a task routinely undertaken by operational forecasters.

5. ACKNOWLEDGEMENTS

This work was supported in part by grants ATM-0240869 and ATM-0240269 from the National Science Foundation and grants N00014-04-10539 and N00014-05-WR20319from the Office of Naval Research.

6. REFERENCES

Babin, S. M., T. D. Sikora, and N. S. Winstead, 2003: A case study of satellite synthetic aperture radar signatures of spatially evolving atmospheric convection over the western Atlantic Ocean. *Boundary-Layer Meteorol*., **106**, 527-546.

Fetterer, F., D. Gineris, and C. C. Wackermann, 1998: Validating a scatterometer wind algorithm for ERS-1 SAR. *IEEE Trans. Geosci. and Remote Sensing*, **36**, 479 – 492.

Foster, R., T. D. Sikora, and G. S. Young, 2004: The correction of surface layer wind speeds for atmospheric stratification and height. *Proc. Second Workshop on Coastal and Marine Applications of SAR*, Svalbard, Norway, 2003 September, European Space Agency SP-565, 39-47.

Freilich, M. H. and R. S. Dunbar, 1999: The accuracy of the NSCAT-1 vector winds: Comparisons with National Data Buoy Center buoys. *J. Geophys. Res*., **104**, 11,231–11,246.

Gerling, T., 1986: Structure of the surface wind field from the SEASAT SAR. *J. Geophys. Res*., **91**, 2308-2320.

Hersbach, H., 2003: An improved geophysical model function for ERS C-band scatterometry. ECMWF Technical Memorandum 395.

Horstmann, J., W. Koch, S. Lehner, and R. Tonboe, 2000: Wind retrieval over the ocean using synthetic aperture radar with C-band HH polarization. *IEEE Trans. Geosci. and Remote Sensing*, **38**, 2122 – 2131.

Horstmann, J., J. Schiller, J. Schulz-Stellenfleth, and S. Lehner, 2003: Global wind speed retrieval from SAR. *IEEE Trans. Geosci. Remote Sens*., **41**, 2277 – 2286.

Johannessen, O. M., H. Espedal, B. Furevik, D. Akimov and A. Jenkins, 1999: COAST WATCH: Integrating satellite SAR in an operational system for monitoring coastal currents, wind, Surfactants and oil spills: Proc. Second International Conference on EuroGOOS, Rome, Italy, pp. 11-13.

Lee, D. L., and R. B. Wilhelmson, 1997: The Numerical Simulation of Non-Supercell Tornadogenesis, Part I: Initiation and Evolution of Pretornadic Misocyclone Circulations along a Dry Outflow Boundary. *J. Atmos. Sci*., **54**, 32-60.

Loescher, K., G. S. Young, B. A. Colle, and N. S. Winstead, 2005: Climatology of barrier jets along the Alaskan coast, Part 1: Spatial and temporal distributions. in press *Mon. Wea. Rev.*

Monaldo, F. M., D. R. Thompson, R. C. Beal, W. G. Pichel, P. Clemente-Colon, 2001: Comparison of SAR-derived wind speeds with model predictions and ocean buoy measurements. *IEEE Trans. Geosci. Remote Sens.*, **39**, 2587-2600.

_____, D. R. Thompson, W. G. Pichel and P. Clemente-Colón, 2004: A systematic comparison of QuikSCAT and SAR ocean surface speeds. *IEEE Trans. Geosci. Remote Sens.*, **42**, 283-291.

Parsons, D. B., and P. V., Hobbs, 1983: The Mesoscale and Microscale Structure and Organization of Clouds and Precipitation in Midlatitude Cyclones. XI: Comparisons between Observational and Theoretical Aspects of Rainbands. *J. Atmos. Sci*., **40**, 2377–2398.

Schär, C., R. B. Smith, 1993: Shallow-water flow past isolated topography. Part I: Vorticity production and wake formation. *J. Atmos. Sci*., **50**, 1373-1400.

Sikora, T. D., G. S. Young, R. C. Beal, F. M. Monaldo, and P. W. Vachon, 2005: Applications of synthetic aperture radar in marine meteorology. Atmosphere Ocean Interactions - Volume 2, W. Perrie, Ed., WIT Press, in press.

Sikora, T. D., G. S. Young and N. S. Winstead, 2006: A novel approach to wind speed analysis using synthetic aperture radar. *Wea. Forecasting,* in press.

Sikora, T. D., G. S. Young, R. C. Beal, and J. B. Edson, 1995: Use of spaceborne synthetic aperture radar imagery of the sea surface in detecting the

presence and structure of the convective marine atmospheric boundary layer. *Mon. Wea. Rev.*, **123**, 3623-3632.

Stoffelen, A. and D. L. T. Anderson, 1993: Wind retrieval and ERS-1 scatterometer radar backscatter measurements. *Advance Space Research*, **13**, 53-60.

_____, and _____, 1997: Scatterometer data interpretation: Estimation and validation of the transfer function *CMOD4. J. Geophys. Res.*, **102**, 5767-5780.

Thompson, D. R. and R. C. Beal, 2000: Mapping high resolution wind fields using synthetic aperture radar. *Johns Hopkins APL Technical Digest*, **21**, 58-67 (Jan-Mar).

Thompson, D. R., F. M. Monaldo, W. G. Pichel, and P. Clemente-Colón, 2001: Combined estimates improve high-resolution coastal wind mapping. *EOS Trans. AGU*, **82**, 469.

Vachon, P. W., Johannessen, J. A., D. P. Browne, 1995: ERS-1 SAR signatures of atmospheric gravity waves. *IEEE Trans. Geosci. Remote Sens*., **33**, 1014-1025.

Wackermann, C. C., C. L. Rufenach, R. A. Schuchman, J. A. Johannesen and K. L. Davidson, 1996: Wind vector retrieval using ERS-1 synthetic aperture radar imagery. *J. Geophys. Res*., **34**, 1343 – 1352.

Weissman, D. E., M. A. Bourassa, and J. Tongue, 2002: Effects of rain rate and wind magnitude on SeaWinds scatterometer wind speed errors. *J. Atmos. Oceanic Technol*., **19**, 738–746.

Winstead, N. S., T. D. Sikora, D. R. Thompson and P. D. Mourad 2002: Direct influence of gravity waves on surface-layer stress during a cold air outbreak, as shown by synthetic aperture radar. *Mon. Wea. Rev*., **130**, 2764-2776.

Young, G. S., T. D. Sikora, and N. S. Winstead, 2005: Use of synthetic aperture radar in fine-scale surface analysis of synoptic-scale fronts at sea. , *Wea. Forecasting*, **20**, 311-327.